# Small-angle scattering tomography of precipitation-hardened multilayer Al/Al-Zn/Al model alloys



Okuda, Hiroshi; Lin, Shan; Nishikawa, Yukihiro

Applied Physics Express

The Japan Society of Applied Physics

LETTER • OPEN ACCESS

# Small-angle scattering tomography of precipitation-hardened multilayer Al/Al-Zn/Al model alloys

Applied Physics Express 12, 105503 (2019) LETTER
https://doi.org/10.7567/1882-0786/ab43ce

# Small-angle scattering tomography of precipitation-hardened multilayer Al/Al-Zn/Al model alloys

Hiroshi Okuda[1*], Shan Lin[1], and Yukihiro Nishikawa[2]

[1]Department of Materials Science and Engineering, Kyoto University, Kyoto 606-8501, Japan
[2]Kyoto Institute of Technology, Sakyo-ku Kyoto 606-8550, Japan

*E-mail: okuda.hiroshi.5a@kyoto-u.ac.jp

Received August 11, 2019; revised September 2, 2019; accepted September 11, 2019; published online September 20, 2019

Tomographic images constructed from small-angle X-ray scattering (SAXS) intensities utilizing microbeams have been examined for a model multilayered aluminum alloy sample heat-treated to form spatially modulated composition and microstructures. Spatial distributions of composition and precipitation microstructure have been examined by one-dimensional scanning SAXS measurements and two-dimensional tomographic images of attenuation parameters and integrated intensity of SAXS intensity. Reconstructed images using the integrated intensity reflected the distribution of precipitates in terms of their volume fraction over the sample inside the sample, and agreed with more detailed analysis made in the one-dimensional case. © 2019 The Japan Society of Applied Physics

Aluminum based age hardenable alloys, e.g., Al–Mg–Zn–Cu,[1,2] Al–Li–Cu,[3] Al–Mg–Si[4,5] alloys, play important roles in designing an energy-efficient transportation system. Such alloy systems have been applied to, for example, high speed trains,[6] automobiles,[7] and aircrafts.[8] Although the peak strength of these alloys after optimized heat-treatment sometimes reached close to 1 GPa level,[9,10] requirements on the materials are often not on a single property but a combination of several properties, some of which are challenging to be compatible in nature, such as ductility, strength, hardness, humidity-resistance, excellent mechanical properties and low cost. One of the solutions to the requirements is to design composite materials that combine several materials that have different properties[11,12] at a reasonable cost. Combination of different Al-based alloys realized by multilayered structures have been proposed[13,14] aiming at rapid and large age-hardenability. In such alloys, spatially modulated composition induces microstructures whose local strength, or the precipitation microstructure, changes with position. To examine such samples, small-angle X-ray scattering (SAXS) measurements with an X-ray microbeam is an attractive solution, since the SAXS pattern gives information on nanostructure of the region illuminated by the beam, where the size of the microbeam may be small enough to study compositional modulation, and still view large landscape up to a mm by scanning the beam in the sample. For example, Sato et al.[14] examined Al-Mg/Al-Zn 5 alternative multilayer sheets by scanning SAXS. Such one-dimensional scanning measurements can be useful to understand spatially modulated nanostructures,[14–18] if the multilayer sheets are homogeneous along the beam, and changes only in the direction normal to the layer interface in the edge-view configurations. In some cases, the distribution is heterogeneous in-plane, sometimes due to undulation or local damage during rolling or additional processes such as machining, jointing, or welding. Examining the nanostructure distribution in such samples is useful in anticipating mechanical properties of such complex structures. Computed tomography (CT) is a powerful tool to examine such heterogeneity existing inside the sample, and widely used from biomedical applications/diagnosis[19–21] to materials science,[22,23] where the measured data comprised of a set of scalar quantity. Successful analysis have been reported for SAXS tomography of biomedical/softmatter materials which are weakly absorbing objects.[24–27] In the present work, we performed simultaneous measurements of attenuation and SAXS, and showed the distribution of attenuation, related to the concentration distribution of Zn, and that of integrated intensity obtained from SAXS, related to the volume fraction of the precipitates, and presented a two-dimensional distribution of these quantities calculated from the filtered backprojection (FBP) method.[28,29]

Present measurements have been performed at beam-line 40XU of SPring-8, Japan. X-rays with the photon energy of 15 keV have been collimated by a pinhole with a diameter of 20 micrometers, and introduced to a sample stage. Schematic illustrations of the present measurements are shown in Fig. 1. Samples are placed at the center of rotation stage fixed on a translation stage. At each translation position $u$, the sample was rotated from $\theta = 0$ degree to 180 degrees and measured at every 3 degrees, with translation step of 20 micrometers. The transmitted beam was monitored by an ionization chamber and a photo diode, and the SAXS intensity was measured by a Pilatus 100k detector set its longer side of sensor area parallel to the rotation axis of the sample stage.

In the present work, a model age-hardenable alloy of Al/Al-Zn/Al alloy three-layered sheet with nominal thickness of 0.5 mm was heat-treated at 773 K for 4 h to form a compositional gradient inside the sample by interdiffusion. Then the sample was cut into a rod with a width of approximately 0.6 mm, solution treated at 573 K for 5 min and quenched into iced water. After aging treatment of 24 h at 313 K, the sample contain Guinier-Preston (GP) zones where the spatial distribution may vary depending on the compositional modulation.

Figure 2(a) shows the SAXS intensity after correction with respect to transmission, background and fluorescence, shown for each positions with $\theta = 0$, giving the sum of SAXS profile of the voxels along the direction parallel to the surface ($x$ direction in Fig. 1); this corresponds to the one-dimensional scanning SAXS after subtraction of the background and fluorescent intensity, $I_{BG}(q)$ and $I_{FL}(q)$. Since the

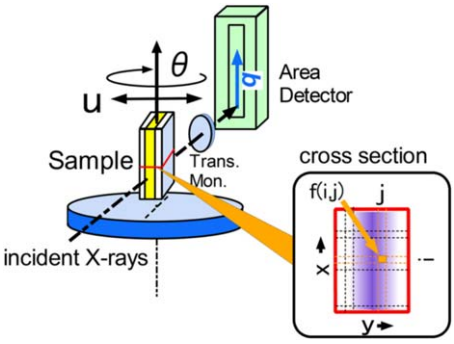


**Fig. 1.** (Color online) Schematic illustration of the present measurement system.

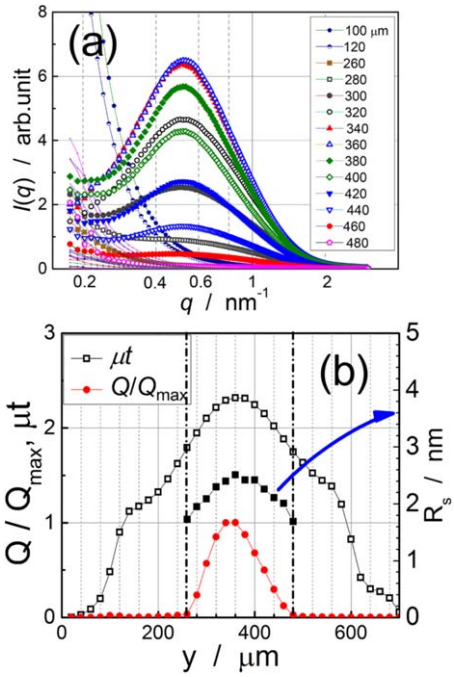


**Fig. 2.** (Color online) SAXS profiles during one-dimensional scanning along *y*-axis (a) and the attenuation parameter, $\mu t$, integrated intensity, Q, and spherical radius, Rs obtained from the one dimensional scan (b).

measured SAXS intensity, $I_{obs}(q)$ is related to the normalized SAXS intensity, $I_{coh}(q)$ by

$$I_{obs}(q) = tTI_{coh}(q) + TI_{BG}(q) + T'I_{FL} \quad (1)$$

with

$$I_{coh}(q) = I_{GP}(q) + I_{def}(q) + I_{DB}(q)$$

where $T = (I_1/I_0) = \exp\left\{-\int_0^{t_0} \mu(t)dt\right\}$ is the transmission, $I_0$ and $I_1$: the intensity of the incident beam and transmitted beam respectively: $t$ the sample thickness, $\mu$ and $\mu'$: the linear absorption coefficient for the incident and Zn fluorescense photon energy. T′ is an effective transmission for fluorescent X-rays defined by,

$$T' = T\int_0^{t_0}\left[\exp\left[-\int_{t'}^{t_0}\{\mu'(t) - \mu(t)\}dt\right]\right]dt'.$$

Coherent SAXS intensity contains the intensity from GP zones ($I_{GP}$), lattice defects and grain boundary oxides ($I_{def}$), and parasitic scattering mainly by double Bragg reflections and surface scattering ($I_{DB}$). The latter two components have quite different shape (streaks) and/or q-range (far low angle regions) from $I_{GP}(q)$ in the present case, and subtracted from the intensity. SAXS intensity profiles between $y = 280\ \mu$m and $y = 460\ \mu$m shows a peak around $q = 0.5\ \text{nm}^{-1}$, known as characteristic for cluster systems with moderately large volume fractions.[30–33] In contrast, very strong scattering profiles at $y = 100\ \mu$m and $y = 120\ \mu$m are due to the parasitic scattering at the sample surface, and removed from the analysis. The distribution of attenuation parameter, $\mu t$, in Fig. 2(b) shows a bell-shaped peak between $y = 140\ \mu$m and $y = 560\ \mu$m, suggesting that Zn atoms spread out close to the sample edge by interdiffusion. Still, the integrated intensity, $Q$, which is related to the SAXS intensity from GP zones, $I_{GP}(q)$ and precipitation microstructural parameters by

$$Q = 4\pi\int_0^{\infty} q^2 I_{GP}(q)\mathrm{d}q = \Delta\rho^2 V_f(1 - V_f), \quad (2)$$

takes a positive value only in the vicinity of the sample center. Here, $\Delta\rho$ is the electron density contrast between the GP zones and the matrix, $V_f$ is the volume fraction of the GP zone. For small $V_f$, $Q$ is approximately proportional to $V_f$. Since the composition of the precipitate is known to be the same over the sample,[30] normalized $Q$ in Fig. 2(b) represents the change in the volume fraction of the GP zones. The integrated intensity disappears at $y = 230\ \mu$m and $y = 480\ \mu$m, suggesting that precipitates exist only inside this region, and the change in the attenuation parameters in the outer region should be attributed either by Zn concentration in the solid solution state, or heterogeneity of the outer shape of the sample. Simple one-dimensional scanning measurement is not enough to conclude the question. The spherical radius, $R_s$, obtained by the Guinier approximation[30–33] of $I_{coh}(q)$ in Fig. 2(a),

$$I_{coh}(q) = I_0 S(q)\exp(-R_s{}^2q^2/5) \quad (3)$$

is also shown as the average radius in the figure, where $S(q)$ is the structure function giving interference between neighboring GP zones, and evaluated by recursive procedure on $R$s and $S(q)$.[31,33] The average size of the precipitates is largest at the peak composition, which is reasonable considering the composition-dependent coarsening rate of the precipitates.[34]

To reconstruct the tomographic picture by standard FBP methods,[28,29] the quantity used for the tomographic calculation need to have a linear character, i.e.

$$\mathrm{f}(u, \theta) = \sum_{u,\theta} f(i, j). \quad (4)$$

For example, attenuation constant, $\mu t$, satisfies the relationship because

$$-\ln(T(u, \theta)) = \int_{u,\theta} \mu(i, j)dr \sim \sum_{u,\theta} \mu(i, j) \quad (5)$$

Similarly, the integrated intensity also satisfies the same relationship as

$$\mathrm{Q}(u, \theta) = \frac{1}{T(u, \theta)}\int_{u,\theta} 4\pi q^2 I_{i,j}(q)dq = \sum_{u,\theta} Q(i, j) \quad (6)$$

where $\mu$(i,j), $Q$(i,j), and $I_{ij}$(q) belong to the voxel (i,j). It should be noted that $I_{ij}(q)$ need to be taken with the scattering vector, $q$, parallel to the rotation axis. Sum is taken at a fixed u and along a fixed $\theta$. Figure 3(a) and 3(b) give CT images

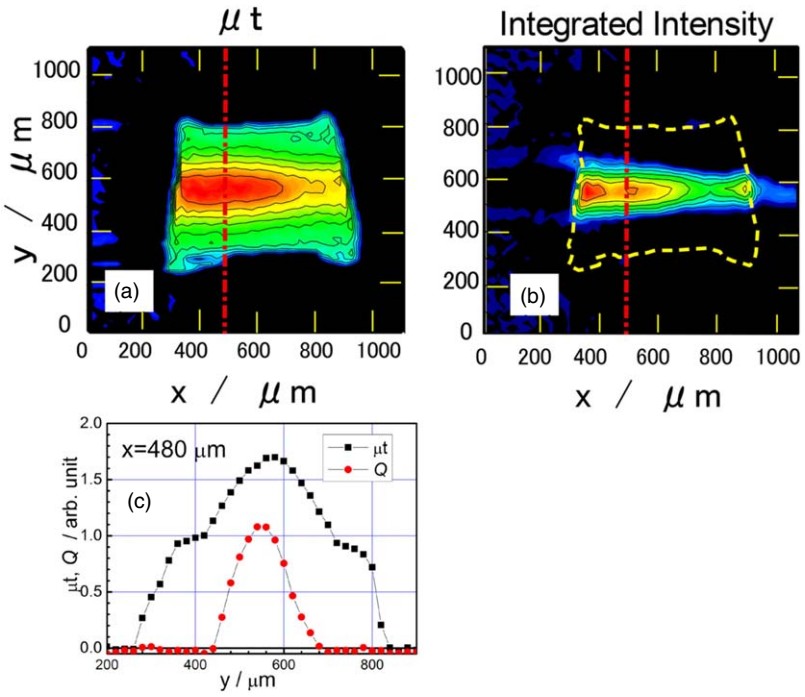


**Fig. 3.** (Color online) Reconstructed images of composition (attenuation) and volume fraction (integrated intensity) of the sample. Broken line in (b) is the outer shape of the sample obtained from absorption (normal) CT in (a). The cross section profile along the red dotted line is shown in (c).

using the attenuation constant, $\mu t$, and the integrated intensity, $Q$. The integrated intensity was calculated after subtraction of SAXS components other than precipitates. The reconstructed image of attenuation shows that the outer shape of the sample is slightly deformed at the corner, and the Zn concentration is not uniform in the in-plane ($x$) direction. The map obtained for the integrated intensity shows nontrivial value in the region only close to the center of the sample, where the Zn concentration is high, and the in-plane heterogeneity is similar to that of the attenuation map. From the reconstructed maps, we concluded that the present sample is not heterogeneous in the in-plane direction, both in concentration and precipitation, and therefore the one dimensional analysis shown in Fig. 2 gave the nanostructure average over some extent of different compositions. A similar comparison to Fig. 2(b) is shown in Fig. 3(c), which was cut at a fixed position, $x = 480\ \mu$m of the maps. Although the statistics is not as good as Fig. 2, the figure suggests a Gaussian shaped Zn concentration. Concerning the distribution of $R_s$, the approach used for the volume fraction map is not applicable since the Guinier radius, which has a statistical meaning as[30)]

$$R_s^2 = \frac{\int_v R^8 f_i(R)\,dRdt}{\int_v R^6 f_i(R)\,dRdt} \tag{7}$$

requirement on linear relationship of Eq. (4) is not fulfilled. In principle, $Q$(i,j) can be calculated either by FBP process of $I(q)$ into $I_{ij}(q)$ first and then integration at each voxel, or integrate to obtain $Q(u,\theta)$ first and then FBP process to obtain $Q$(i,j). Present work adopted the latter for better stability of the solution. However, the FBP process of $I(u,\theta,q)$ needs to be made first, and then $R$s at each voxel can be calculated from SAXS profile mapped for each voxel. However, the data statistics is not good enough to evaluate the slope of a decomposed SAXS map in the present measurement, and left for future measurements.

Tomographic analysis has been made for a model Al/Al-Zn/Al sample after heat treatment. Simultaneous transmission and SAXS measurements of about 3000 exposures resulted in mapping of Zn concentration and Zn-rich precipitates that contribute to hardening of the material in success. Present result opens a new approach of nondestructive (pre-deformation) evaluation of mechanical properties of precipitation hardened composite materials having complex shape, a useful tool for designing structural components.

**Acknowledgments** The present work has been supported by grant-in-aid for scientific research from JSPS, proposal number 18K18944 and 18H05476. SAXS measurements have been performed under proposal numbers 2016A1168, 2016B1275, 2016B1282, 2017A1570 of SPring-8. The authors acknowledge technical support by Mr K. Aoyama of JASRI during the measurements at BL40XU, SPring8.

1) M. Dumont, W. Lefabre, B. Doisneau-Cottingnies, and A. Deschamps, Acta Mater. **53**, 2881 (2005).
2) T. Marlaud, A. Deschamps, F. Bley, W. Lefebre, and B. Baroux, Acta Mater. **58**, 248 (2010).
3) P. Donnadieu, Y. Shao, F. DeGeuser, G. A. Botton, S. Lazar, M. Cheynet, M. de Boissieu, and A. Dechamps, Acta Mater. **59**, 462 (2011).
4) G. A. Edwards, K. Stiller, G. L. Dunlop, and M. J. Couper, Acta Mater. **46**, 3893 (1998).
5) A. Serizawa, S. Hirosawa, and T. Sato, Metall. Mater. Trans. A **39**, 243 (2008).
6) K. Horihata, H. Sakamoto, H. Kitabayashi, and A. Ishikawa, Hitachi Rev. **57**, 18 (2008) [in Japanese].
7) K. Chiba, Keikinzoku **56**, 136 (2006) [in Japanese].
8) A. S. Warren, Proc. 9th Int. Conf. Aluminum Alloys (Brisbaine, Australia), 2004 24.
9) A. Inoue, K. Ohtera, A. P. Tsai, and T. Masumoto, Jpn. J. Appl. Phys. **27**, L479 (1988).
10) K. Osamura, O. Kubota, P. Promstit, H. Okuda, S. Ochiai, K. Fujii, J. Kusui, T. Yokote, and K. Kubo, Metall. Mater. Trans. A **26**, 1597 (1995).

11) T. W. Clyne, in *Physical Metallurgy*, ed. R. W. Cahn and P. Haasen, (Elsevier, Amsterdam, 1996) 4th Ed., p 2567–625.
12) T. W. Clyne and P. J. Withers, *An Introduction to Metal Matrix Composites* (Cambridge University Press, Cambridge, 1993).
13) J. E. Hatch (ed.) *Aluminum:Properties And Physical Metallurgy* (ASM, Washington, DC, 1984), pp. 371–4.
14) K. Sato, K. Matsumoto, and H. Okuda, Mater. Trans. **60**, 254 (2019).
15) S. Rinnerthaler, P. Roschger, H. F. Jakob, A. Nader, K. Klaushofer, and P. Fraztl, Calcif. Tissue. Int. **64**, 422 (1999).
16) I. Murase, H. Okuda, R. Kurosaki, S. Ochiai, Y. Yokoyama, K. Inoue, and J. Metastable, Nanocrystall. Mater **24–25**, 213 (2005).
17) F. de Geuser, M. Malard, and A. Deschamps, Phil. Mag. **94**, 1451 (2014).
18) S. Lin, H. Okuda, K. Sato, and K. Matsumoto, submitted to Mater. Trans.
19) A. Mamourian et al. (ed.) *CT Imaging, Practical Physics, Artifacts and Pitfalls* (Oxford University Press, Oxford, 2013).
20) M. J. Budoff and J. S. Shinbane (ed.) *Cardiac CT Imaging* (Springer, Berlin, 2016).
21) [http://fda.gov/radiation-emitting-products/medical-x-ray-imaging/computed-tomography-ct].
22) V. Mazars, O. Caty, G. Ciyegnat, A. Bouterf, S. Roux, S. Denneulin, J. Paihes, and G. L. Vignoles, Acta Mater. **140**, 130 (2017).
23) H. Toda, Z. Azri, B. Shamsudin, K. Shimizu, A. Tkeuchi, K. Uesugi, Y. Uesugi, M. Nakazawa, Y. Aoki, and M. Kobayashi, Acta Mater. **61**, 2403 (2013).
24) P. Fraztl, Nature **527**, 308 (2015).
25) F. Schaff, M. Bech, P. Zaslansky, C. Jud, M. Liebi, M. Guizar-Sicairos, and F. Pfeiffer, Nature **527**, 353 (2015).
26) C. G. Schroer, M. Kuhlmann, S. V. Roth, R. Gehrke, N. Stribeck, A. Almendarez-Camerillo, and B. Lengeler, Appl. Phys. Lett. **88**, 164102 (2006).
27) M. Liebi, M. Georgiadis, A. Menzel, P. Schneider, J. Kohlbrecher, O. Bunk, and M. Guizar-Sicairos, Nature **527**, 349 (2015).
28) T. Saito, *Gazo Shori Arugorizumu* (Kindai Kagaku sha, Tokyo, 1993) [in Japanese].
29) G. T. Herman, *Fundamentals of Computerized Tomography* (Springer, London, 2009).
30) V. Gerold, Phys. Stat. Solidi **1**, 37 (1961).
31) A. Guinier and G. Fournet, *Small-Angle Scattering of X-rays* (Wiley, New York, 1955).
32) P. A. Rikvold and J. D. Gunton, Phys. Rev. Lett. **49**, 286 (1982).
33) S. Pedersen, Phys. Rev. **B47**, 657 (1993).
34) H. Okuda and K. Osamura, J. Inst. Metals **49**, 825 (1985).